

# Data based method for $Z \rightarrow \mu^+\mu^-$ background subtraction in ATLAS detector at LHC

Simonetta Gentile<sup>1</sup>

Halina Bilokon<sup>2</sup>, Vitaliano Chiarella<sup>2</sup>, Giovanni Nicoletti<sup>2</sup>

(1) *Dipartimento di Fisica, Università La Sapienza, Sez. I.N.F.N., Roma,*

(2) *Laboratori Nazionali di Frascati, I.N.F.N., Frascati, Roma.*

## Abstract

The most copious background in the search of much new physics beyond Standard Model results from the production of the resonant  $b\bar{b}Z \rightarrow \mu^+\mu^-$  final state. In order to evaluate and control this background an experimental method is proposed, following a preliminary study [1].

The method takes advantage from the large suppression of the electron decay channel for the signal to be searched, and from the universality of the weak coupling in  $Z$  decay.

The method is based on the study of a sample of experimental data, for the channel  $b\bar{b}Z \rightarrow e^+e^-$ , not depending on the background channel itself, and in principle avoiding theoretical uncertainties and their propagation to Monte Carlo. The different impact of *inner bremsstrahlung* (IB) and of detector response on the measured rates of  $Z$  decays to electrons and muons is investigated using a full simulation of the ATLAS detector. The extension to other final states as  $\tau^+\tau^-$  and heavy flavours, is straightforward.

# 1 Introduction

The production and decay of Z bosons may constitute an irreducible background in the search for new physics beyond the Standard Model.

In hadron collisions in the TeV region, as at Large Hadron Collider(LHC), the theoretical cross sections of Z production as well of other Standard Model processes suffer, at this moment, from large uncertainties. Therefore, the *a priori* evaluation with Monte Carlo techniques of the background suffers from the same uncertainties.

For a better understanding of the problem, as an example, we consider the search of Minimal SuperSymmetric neutral Higgs, namely h (CP-even) and A (CP-odd) decaying to  $\mu^+\mu^-$ ,  $h/A \rightarrow \mu^+\mu^-$ . Values of  $m_h$  and  $m_A$  less than 92.8 GeV and 93.4 GeV have been excluded at LEP [2]. The search at LHC will extend from these values up to the highest value allowed in this scenario,  $m_h \approx 135$  GeV. In this this search one has to disentangle the signal A,  $h \rightarrow \mu^+\mu^-$  from the  $Z \rightarrow \mu^+\mu^-$  background produced with a cross section, which is approximately hundred times larger than the signal [1], [3].

The Monte Carlo simulation of these processes, taking account of all correction loops, is complex and will demand an enormous theoretical effort and a careful tuning on experimental data. As a consequence, the systematic error in the background evaluation, due to the theoretical uncertainty, has to be taken in account. A review of the up-to-date Monte Carlo implementations for LHC is summarized in Ref. [4].

In this note, a strategy has been developed on the combined use of Monte Carlo and data to allow a realistic evaluation of that background at LHC.

## 2 Method

Fig. 1 and Fig. 2 show diagrams corresponding to Z boson production associated with two b-jets and followed by a decay to  $\mu^+\mu^-$ .

The proposed method exploits the two following points (at the level of particle generation):

- a) the rate of  $A, h \rightarrow e^+e^-$  is expected to be suppressed with respect to the signal  $A, h \rightarrow \mu^+\mu^-$  by a factor  $\left(\frac{m_\mu}{m_e}\right)^2$ ,
- b) the rate of the background  $b\bar{b}Z \rightarrow \mu^+\mu^-$  is equal to the rate of  $b\bar{b}Z \rightarrow e^+e^-$  because of the production diagrams which are the same, and of the lepton coupling universality in the Z decay. As a result, barring detector efficiency factors, the number of  $b\bar{b}Z \rightarrow e^+e^-$  gives directly the number of background events  $b\bar{b}Z \rightarrow \mu^+\mu^-$ .

Unfortunately, the method can't be applied straightforward, because of the different *inner bremsstrahlung* (IB) associated to the two leptons. Moreover the detector response is different depending whether the final state contain electrons or muons. This implies that the number of selected  $e^+e^-$  events has to be corrected for the IB photons (see Section 4) and for the acceptance and resolution of the calorimeter and muon spectrometer (see Section 5) before being used as number of background events.

## 3 Monte Carlo Samples

A sample of Z produced in association with two b-jets and decaying in electron and muon pair has been used in this study. The event generator used is AcerMC(2.3) [5] for  $b\bar{b}Z \rightarrow \mu^+\mu^-$

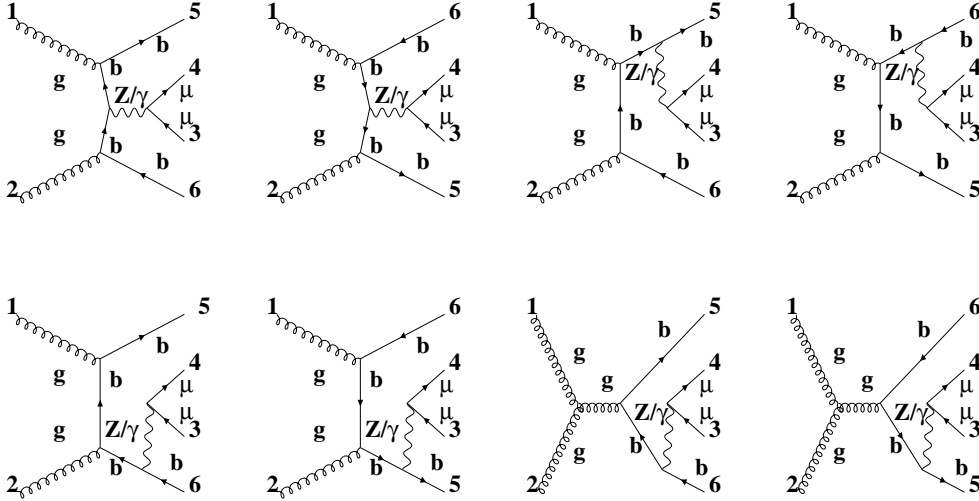


Figure 1: Subset of the diagrams contributing, at “tree level”, to the process  $gg \rightarrow Z/\gamma^* b\bar{b} \rightarrow \mu^+ \mu^- b\bar{b}$ .

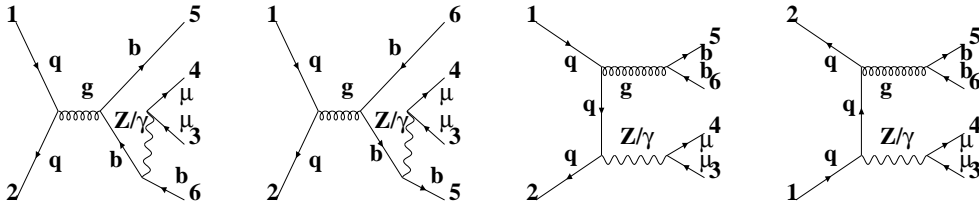


Figure 2: Diagrams contributing, at “tree level”, to the process  $q\bar{q} \rightarrow Z b\bar{b} \rightarrow \mu^+ \mu^- b\bar{b}$ .

and  $b\bar{b}Z \rightarrow e^+e^-$  processes. The hadronization process is described with the PYTHIA(v.6.226) Monte Carlo, whose parameters have been set by ATLAS Collaboration [6]<sup>1)</sup>.

Monte Carlo events are generated for center-of-mass energy,  $\sqrt{s}=14$  TeV. The ATLAS detector response [7] is simulated using the GEANT program [8], [9] which takes into account the effects of energy loss, multiple scattering and showering in the detector, through the ATHENA interface (v.10.01).

A number of events corresponding to three years of data collection with an expected luminosity of  $\int \mathcal{L} dt \approx 30\text{fb}^{-1}$ , have been simulated, that is  $\approx 600000$  events in each of two channels, with a cross section of  $\sigma \approx 22.8\text{pb}$ .

A cut-off  $< 60$  GeV is applied at generator level on the two leptons,  $\ell^+\ell^-$ , invariant mass. A low energy cut is fixed on IB photons at  $P_T > 5$  GeV. This lowest energy to observe a photon cluster in the calorimeter.

<sup>1)</sup>Using PHOTOS package for IB generation.

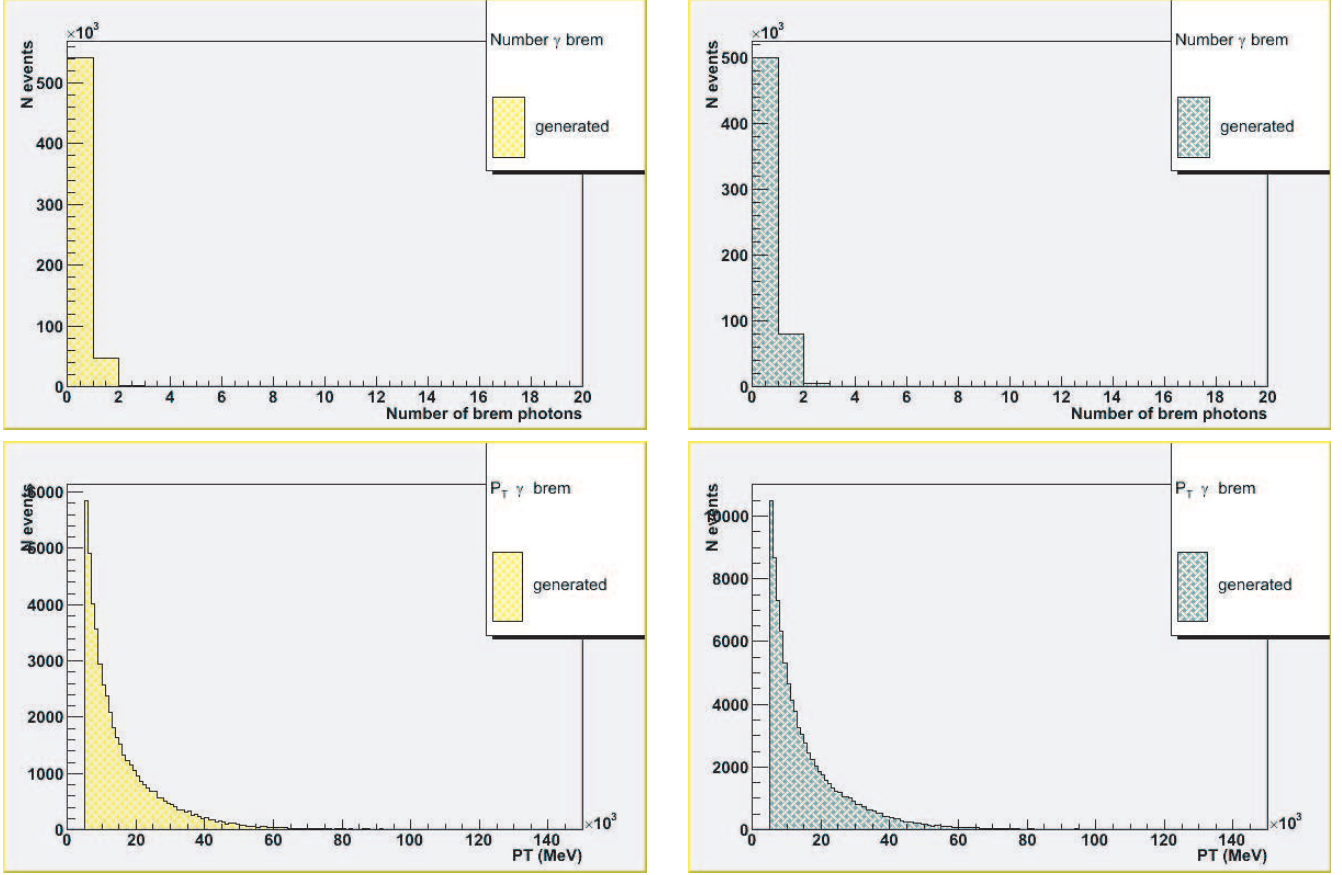


Figure 3: At particle level: a) Number of IB photons in  $b\bar{b}Z \rightarrow \mu^+\mu^-$  (top left). b) Number of IB photons in  $b\bar{b}Z \rightarrow e^+e^-$  (top right). c) Transverse momentum,  $P_T$ , distribution of IB photons in  $b\bar{b}Z \rightarrow \mu^+\mu^-$ ,  $\langle P_T \rangle = 16.18$  GeV (bottom left). d) Transverse momentum,  $P_T$ , distribution of IB photons in  $b\bar{b}Z \rightarrow e^+e^-$ ,  $\langle P_T \rangle = 16.43$  GeV (bottom right).

## 4 Particle Level

In this section the characteristics of the two samples are compared at particle level, before simulating the detector response, and the effect of the *inner bremsstrahlung* is discussed.

The *inner bremsstrahlung* is the emission of photons,  $\gamma_{\text{brem}}$ , near the  $Z e^+ e^-$  or  $Z \mu^+ \mu^-$  vertex. The presence of such photons changes the kinematic configuration of the decay, in particular the lepton 4-momenta. The impact of this effect on the Higgs mass resolution with the ATLAS detector has been studied in Ref. [10]. Here we discuss the IB impact on the most sensitive variable of our analysis, the reconstructed invariant mass,  $M_{\mu^+\mu^-}$  or  $M_{e^+e^-}$ . The same method can be easily extended to any other variable.

### 4.1 IB Photons

Due to the difference between electron and muon mass, more photons are expected to be emitted by electrons than by muons. In Fig. 3, the number of  $\gamma_{\text{brem}}$  is reported for the  $b\bar{b}Z \rightarrow \mu^+\mu^-$  (left) and  $b\bar{b}Z \rightarrow e^+e^-$  (right) samples. The corresponding number of events entering this analysis is listed in Table 1.

The number of events with *bremsstrahlung* photons is larger in  $e^+e^-$  events than in  $\mu^+\mu^-$  as

	bbZ $\rightarrow\mu^+\mu^-$	bbZ $\rightarrow e^+e^-$
$N_{gen}$	590575	586382
$N_{gen}(\gamma_{brem} = 0)$	541425	499939
$N_{gen}(\gamma_{brem} = 1)$	47413	80679
$N_{gen}(\gamma_{brem} = 2)$	1698	5544
$N_{gen}(\gamma_{brem} = 3)$	37	211
$N_{gen}(\gamma_{brem} = 4)$	1	9
$\langle P_T^{\gamma_{brem}} \rangle$ [GeV]	16.18	16.43

Table 1: Number of IB photons,  $\gamma_{brem}$ , at particle level.

expected. In the electron sample, 85.2 % of the events are without IB photons, 13.7 % have 1  $\gamma_{brem}$ , 0.94% 2  $\gamma_{brem}$ . In the muon sample, 91.6% of the events are without IB photons, 8% have 1  $\gamma_{brem}$ , 0.2% 2  $\gamma_{brem}$ .

The average transverse momentum of the radiated photons is close in the two distributions,  $\langle P_T^{\gamma_{brem}} \rangle = 16.18$  GeV for electrons and  $\langle P_T^{\gamma_{brem}} \rangle = 16.43$  GeV for muons, as expected from the *bremstrahlung* energy loss. This result is obtained at particle level without any cut except those mentioned in Section 3, as shown in Fig. 3.

## 4.2 Invariant Mass

The effect of *inner bremstrahlung*, distorting the lepton four momentum, is expected to have some impact on the invariant mass ( $M_{e^+e^-}$ ,  $M_{\mu^+\mu^-}$ ) distributions, different in the two samples. The invariant mass distributions are shown in Fig. 4 (top) for all generated events ( $\mu^+\mu^-$  on the left,  $e^+e^-$  on the right) before correcting for the *bremstrahlung*. The distributions obtained after summing up the four-momentum of  $\gamma_{brem}$  to the total lepton four-momentum are also shown, see Fig. 4 (bottom). The difference due to the *inner bremstrahlung* is not visible, concerning less than 15% of events.

To control the method validity, the distributions of Fig. 4 are shown for the sub-sample of events with at least one radiated photon, see Fig. 5. After including IB photons, the mass distributions are Breit-Wigner shaped. For the same sub-sample, Fig. 6 shows the ratio between the number of events with Z decaying to  $\mu^+\mu^-$  and the number of events with Z decaying to  $e^+e^-$ ,  $\left(\frac{N_{Z\rightarrow\mu^+\mu^-}}{N_{Z\rightarrow e^+e^-}}\right)$  before (blue marks) and after (red marks) the *bremstrahlung* correction. The addition of photon four-momentum reduces the difference between  $M_{e^+e^-}$  and  $M_{\mu^+\mu^-}$  distributions, and the ratio of number of events become more regular.

Fig. 7 in a logarithmic scale shows that the summing of  $\gamma_{brem}$  four momentum moves the events towards higher masses.

The ratios of the invariant mass distributions for muon and electron events, before and after IB correction, are given in Fig. 8 (bottom) for all generated events; there (top and centre) we report as well, for convenience, the information of Fig. 4.

The two ratio distributions are shown overlaid in Fig. 9. The red-dots distribution, corresponding to the corrected invariant mass distribution, shows more stable behavior, that is a necessary condition to evaluate the number of  $Z \rightarrow \mu^+\mu^-$  from the number of  $Z \rightarrow e^+e^-$  produced.

In conclusion, at the generator level the difference due to the *inner bremstrahlung* between

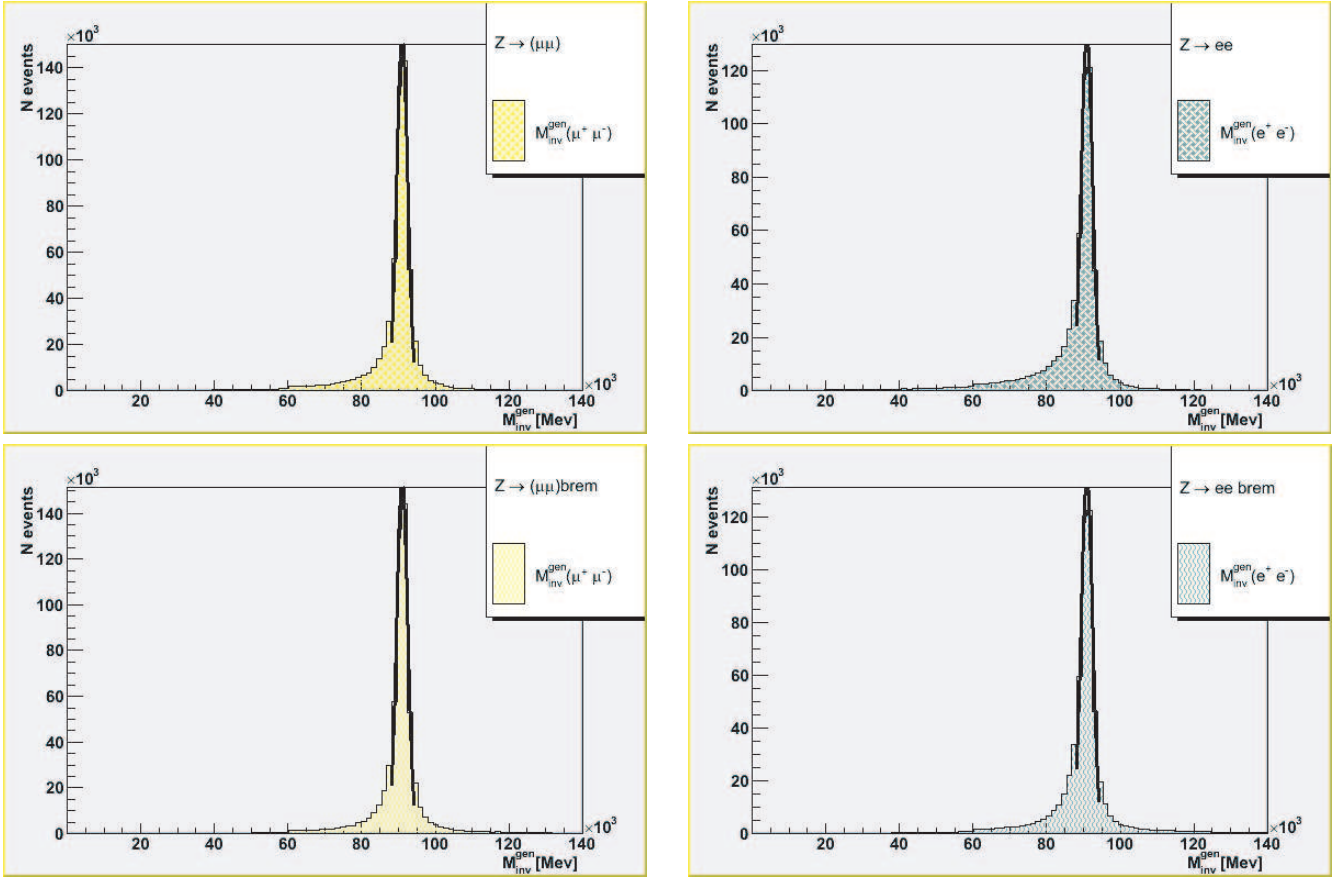


Figure 4: At particle level: distributions of invariant mass  $M_{\mu^+\mu^-}$ ,  $M_{e^+e^-}$  (top). The corresponding quantities  $M_{\mu^+\mu^-\gamma}$ ,  $M_{e^+e^-\gamma}$  after including IB photons (bottom). The gaussian fit is shown as solid line.

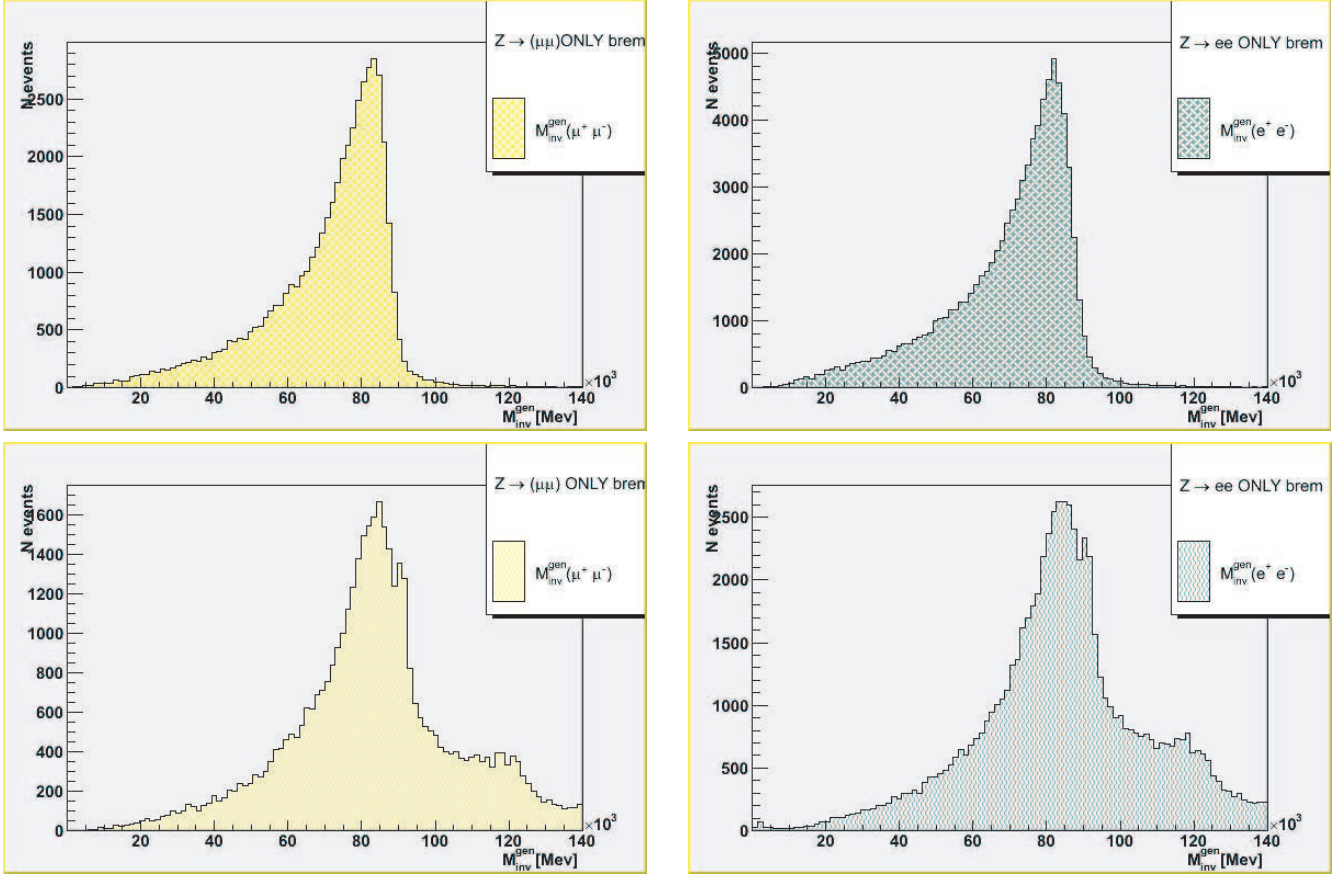


Figure 5: At particle level: distributions of invariant mass  $M_{\mu^+\mu^-}$ ,  $M_{e^+e^-}$  for events containing at least one IB photon (top). The corresponding quantities  $M_{\mu^+\mu^-\gamma}$ ,  $M_{e^+e^-\gamma}$  after correction for IB photons (bottom). The effect of the photon energy cut,  $P_T > 5$  GeV (Section 3), is clearly visible on the right hand side of the distributions

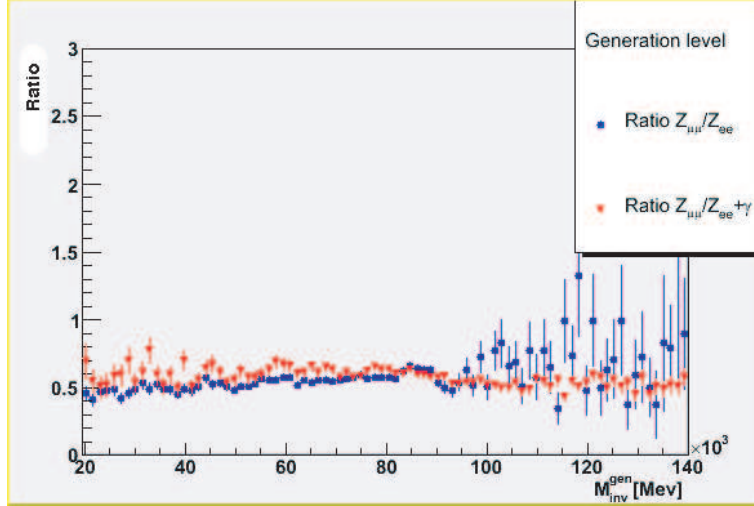


Figure 6: At particle level: ratio between the number of events with  $Z$  decaying to  $\mu^+\mu^-$  and the number of events with  $Z$  decaying to  $e^+e^-$ ,  $\left(\frac{N_{Z\rightarrow\mu^+\mu^-}}{N_{Z\rightarrow e^+e^-}}\right)$ , before IB correction (blue symbols) and after (red symbols). Only events containing a radiated photon are included.

the distributions of  $M_{e^+e^-}$  and  $M_{\mu^+\mu^-}$  reduces to a difference in spread. More precisely the spread decreases from  $\approx \pm 30\%$  to less than  $\approx \pm 12\%$  for masses between 100 and 140 GeV, which implies that correction factors should not be important.

This encouraging result has to be verified after simulation of the detector response to electrons and muons, as will be discussed in the following sections.

## 5 Detector Simulation

After the study of  $b\bar{b}Z\rightarrow\mu^+\mu^-$  and  $b\bar{b}Z\rightarrow e^+e^-$  events at generator level, the effect of the detector response, its acceptance and resolution should be considered. The ATLAS detector response is simulated using ATHENA program, as described in Section 3, including GEANT4, which take in account the effects of energy loss, multiple scattering and showering in the detector. The differences on detection and reconstruction of electrons and muons are discussed in the following section.

### 5.1 Leptons

The electrons and muons involve different detectors, electromagnetic calorimeter and muon spectrometer, implying different momentum resolution, angular acceptance and efficiency. In Fig. 10, the number of muons (on the left) and the number of electrons (on the right) generated and reconstructed is shown. The transverse momentum generated and reconstructed from detector is shown in the lower part of Fig. 10. The average momentum reconstructed is  $\langle P_T \rangle = 37.83$  GeV for muons and  $\langle P_T \rangle = 42.61$  GeV for electrons, respectively. The reconstruction efficiency is higher for muons than for electrons. All distributions shown, either at generator level (hatched color), or after simulation and reconstruction (full color), are without cuts.

The following criteria were followed in the analysis, respectively, for muons and electrons:

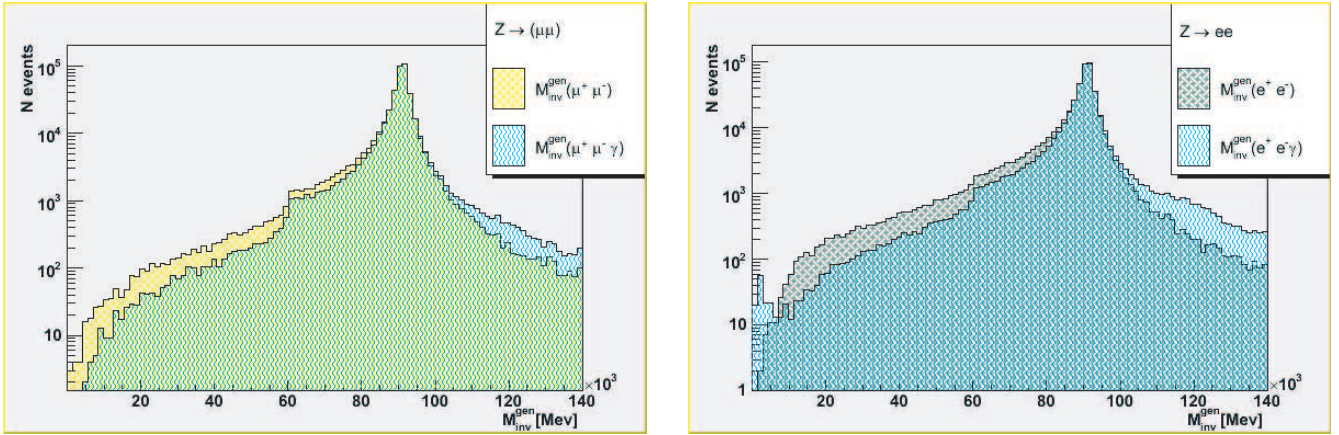


Figure 7: At particle level: distributions of the invariant mass  $M_{\mu^+\mu^-}$  (left),  $M_{e^+e^-}$  (right), for all generated events, before adding IB photons, in yellow ( $\mu^+\mu^-$ ) and green ( $e^+e^-$ ), and afterwards, in light blue ( $\mu^+\mu^-$  and  $e^+e^-$ ).

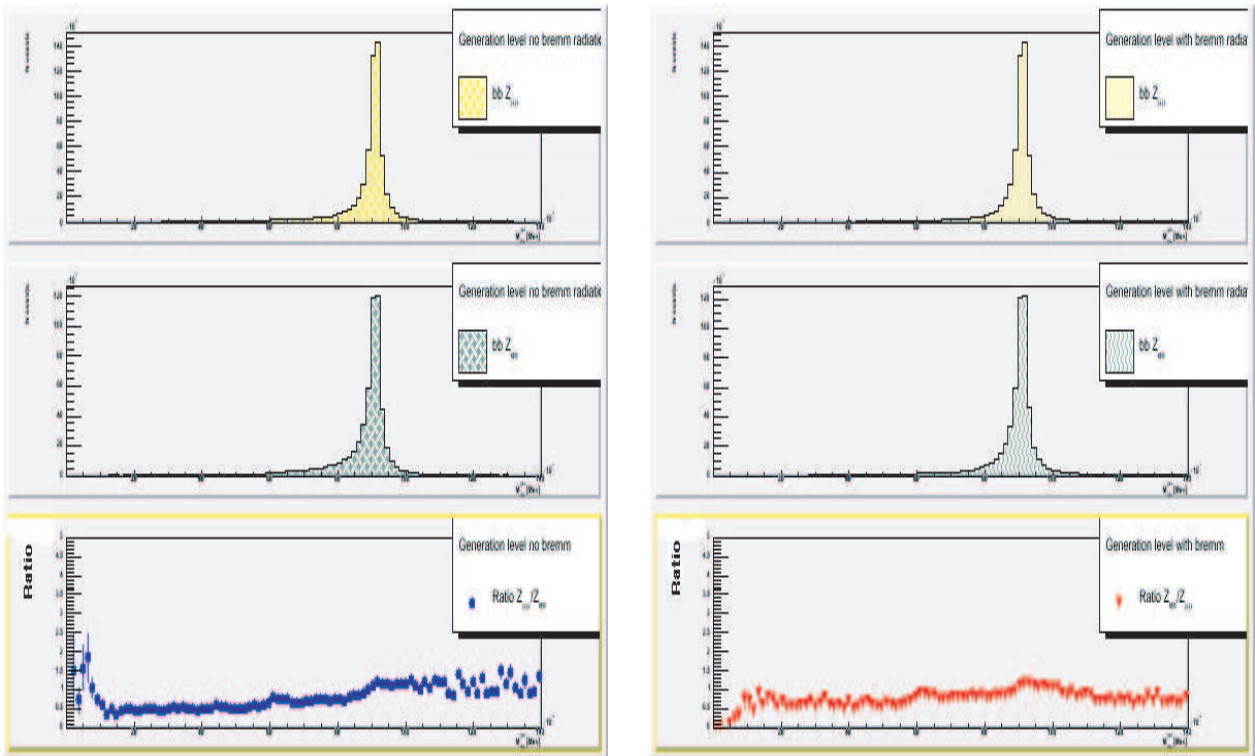


Figure 8: Distributions for all events, at particle level, of the invariant mass,  $M_{\mu^+\mu^-}$  (top),  $M_{e^+e^-}$  (centre), and their ratio (bottom), before adding IB photons (left) and after correcting for them (right).

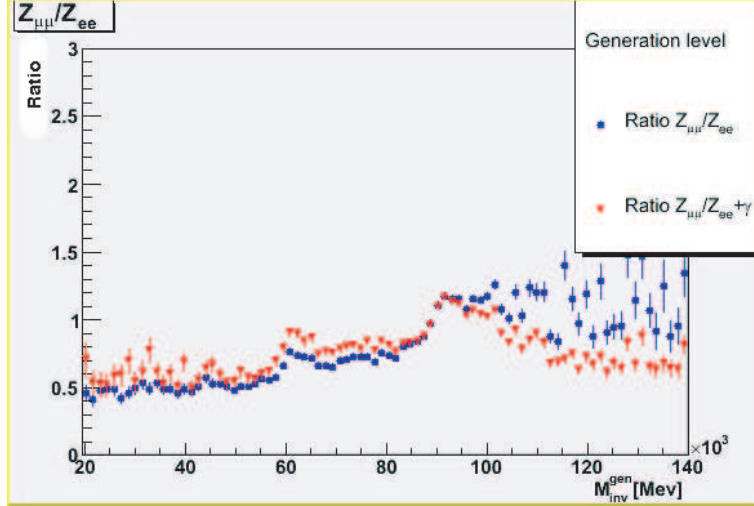


Figure 9: At particle level: ratio between the number of events with  $Z$  decaying to  $\mu^+\mu^-$  and the number of events with  $Z$  decaying to  $e^+e^-$ ,  $\left(\frac{N_{Z\rightarrow\mu^+\mu^-}}{N_{Z\rightarrow e^+e^-}}\right)$ , before IB correction (blue symbols) and after (red symbols). All generated events are included.

- **Muons** are reconstructed as tracks, in both the inner detector and the muon spectrometer (so named combined reconstruction), with  $P_T > 10$  GeV and  $|\eta| < 2.5$ .<sup>2)</sup>
- **Electrons** are reconstructed as clusters, in the electromagnetic calorimeter, with  $P_T > 10$  GeV and  $|\eta| > 2.5$ , with a track associated (inside  $\Delta\eta = 0.025$  and  $\Delta\phi = 0.05$ ). A cluster size of  $5\times 5$  cells is used to measure the electromagnetic energy. To achieve the best performance, the energy measured by the electromagnetic calorimeter and the angles  $(\theta, \phi)$  measured in the tracker, are used.

## 5.2 Photons

An energy deposit in the electromagnetic calorimeter is identified as a photon and used in the analysis if the following conditions are fulfilled.

- **Photons** are reconstructed as clusters in the electromagnetic calorimeter, with  $E_T > 10$  GeV and rapidity  $|\eta| > 2.5$ , without any track associated (inside  $\Delta\eta = 0.025$  and  $\Delta\phi = 0.05$ ). A cluster size of  $5\times 5$  cell is used to measure the electromagnetic energy. If the photon reconstruction efficiency drops in the energy range  $5 \text{ GeV} < E_T < 10 \text{ GeV}$ , the demand to reconstruct the highest possible number of  $\gamma_{\text{brem}}$  suggests the use of the lowest possible threshold.

The number of reconstructed photons (full color) is shown in Fig. 11 compared to the number of generated photons without any cut (hatched). In next section we shall try to identify IB photons among all  $\gamma$ 's of the events.

<sup>2)</sup>The lower  $P_T$  used, with respect to Ref. [3] is to study purposes.

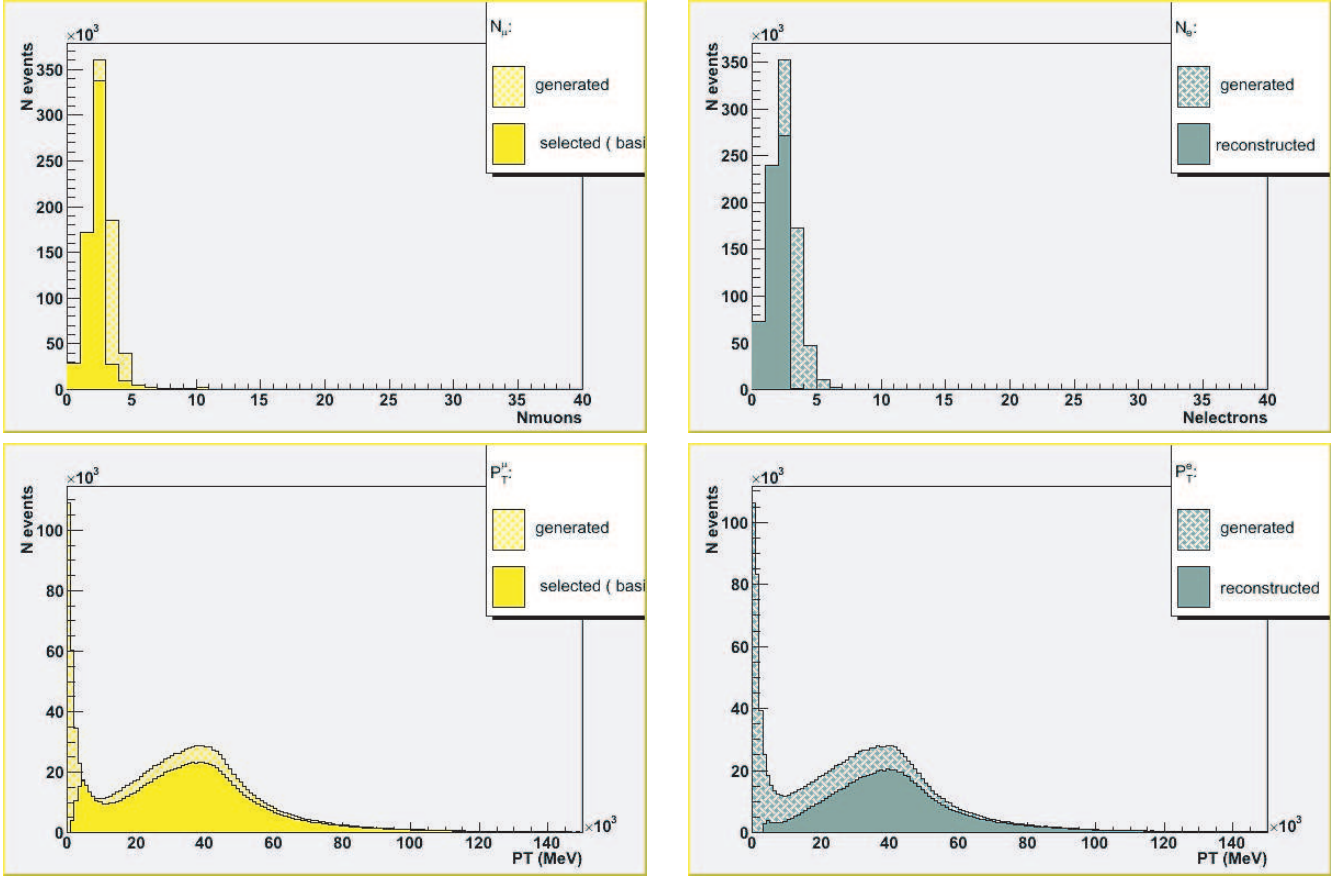


Figure 10: Distributions at generator level (hatched color) and after simulation in the detector and reconstruction (full color), without cuts, for:  
a) Number of muons in  $b\bar{b}Z \rightarrow \mu^+\mu^-$  events (top, left). b) Number of electrons  $b\bar{b}Z \rightarrow e^+e^-$  events (top, right). c) Transverse momentum,  $P_T$ , of muons in  $b\bar{b}Z \rightarrow \mu^+\mu^-$  events (bottom, left). d) Transverse momentum,  $P_T$ , of electrons in  $b\bar{b}Z \rightarrow e^+e^-$  (bottom, right).

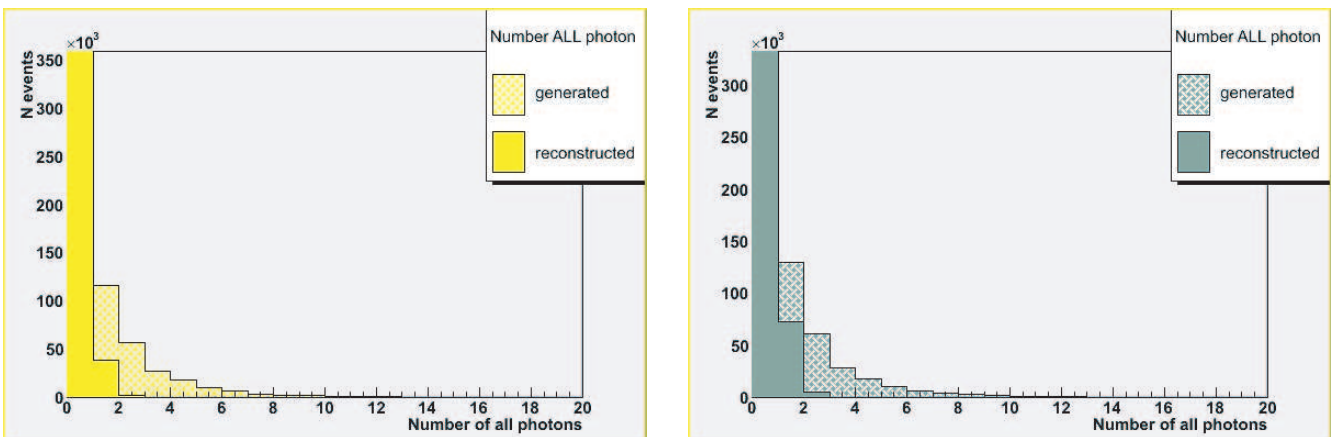


Figure 11: Distributions at generator level (hatched color) and after simulation in the detector and reconstruction (full color), without cuts, are shown for: a) Number of photons in  $b\bar{b}Z \rightarrow \mu^+\mu^-$  events(left). b) Number of photons in  $b\bar{b}Z \rightarrow e^+e^-$  events(right).

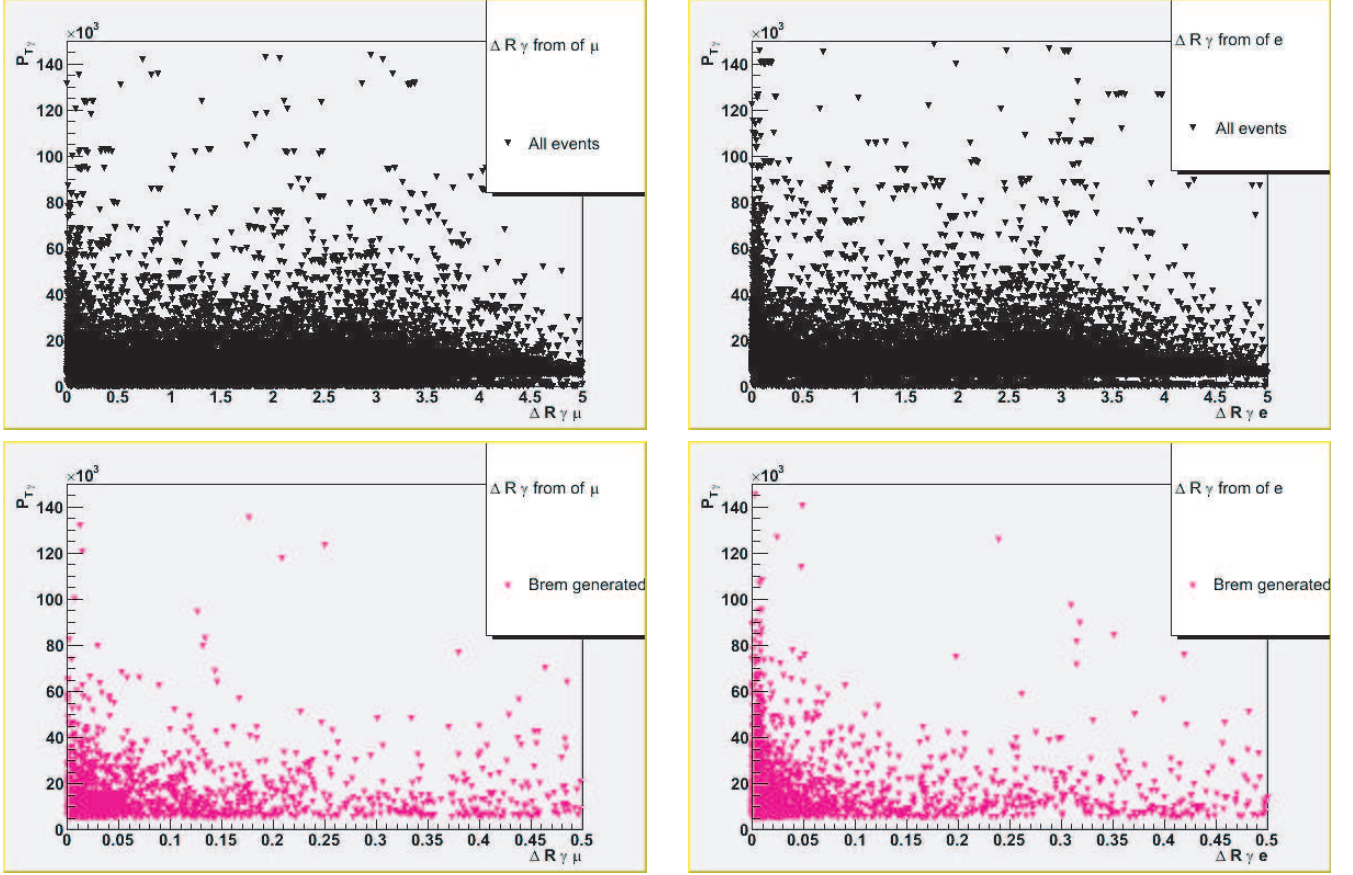


Figure 12: At generator level level: distribution of the transverse momentum,  $P_T$  versus the angular distance between  $\gamma$  and lepton,  $\Delta R$  (see text) a) for all photons in  $b\bar{b}Z \rightarrow \mu^+\mu^-$  events (top, left). b) for all photons in  $b\bar{b}Z \rightarrow e^+e^-$  events (top, right). c) for IB photons in  $b\bar{b}Z \rightarrow \mu^+\mu^-$  events (bottom, left). d) for IB photons in  $b\bar{b}Z \rightarrow e^+e^-$  events (bottom, right). The samples considered for c) and d) are sub-samples of the whole sample ( 25317  $\mu^+\mu^-$  and 24564  $e^+e^-$ ).

### 5.3 Bremsstrahlung Photons Identification

The method described in Section 4, presents an intrinsic difficulty in the application to real data: the identification of IB photons. Their selection from the  $\gamma$  background is based on their different kinematics characteristics.

In Fig. 12, at generator level, the transverse momentum  $P_T^\gamma$  is shown as a function of  $\Delta R = \sqrt{\Delta\eta^2 + \Delta\phi^2}$ , the angular distance between  $\gamma$  and lepton for all photons (upper section) and for IB photons (lower section), respectively for  $\mu^+\mu^-$  and  $e^+e^-$  events. The 2-dimensional plots show no substantial difference in  $P_T$  depending whether the  $\gamma$  was an IB one, or not. It should be noticed that  $\Delta R \approx 0.09$  corresponds to 5x5 times the cluster size (0.125 x 0.125) in the electromagnetic calorimeter of ATLAS.

The distance  $\Delta R$  from lepton is plotted in enlarged scale, at generator level, in Fig. 13 for all photons in  $\mu^+\mu^-$  events (top, left),  $e^+e^-$  events (top, right) and for IB photons in  $\mu^+\mu^-$  events (bottom, left),  $e^+e^-$  events (bottom, right). Based on these considerations, a natural choice is to consider as IB  $\gamma$ 's those in a cone around the lepton direction, with  $\Delta R < 0.15$  for muons and  $\Delta R < 0.25$  for electrons.

The considerations that can be drawn for the two samples are:

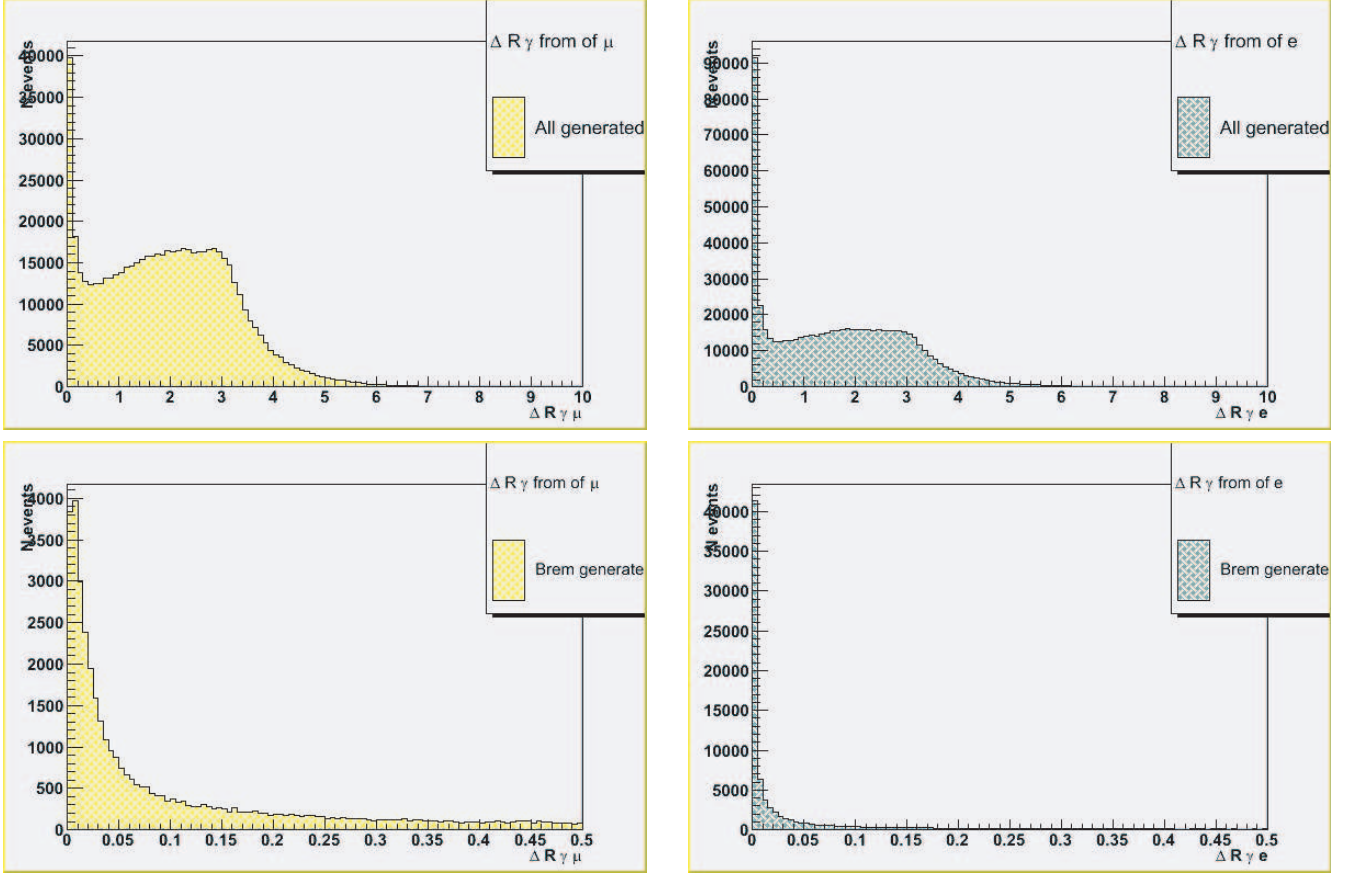


Figure 13: At particle level: distributions of  $\Delta R$ , angular distance between an IB photon and a lepton (see text) a) for all photons in  $b\bar{b}Z \rightarrow \mu^+\mu^-$  events (top, left). b) for all photons in  $b\bar{b}Z \rightarrow e^+e^-$  events (top, right). c) for IB photons in  $b\bar{b}Z \rightarrow \mu^+\mu^-$  events (bottom, left). d) for IB photons in  $b\bar{b}Z \rightarrow e^+e^-$  events (bottom, right) .

- **Electrons.** If the photon is emitted close to an electron in the calorimeter, only one cluster is reconstructed and the combined four-momentum is measured. In this analysis, as already mentioned, the four-momentum of a photon in the angular cone  $\Delta R < 0.15$  is summed up to electron one.
- **Muons.** In the case of muons hard photons with transverse energy  $E_T > 5$  GeV are taken in account in the angular cone  $\Delta R < 0.25$ . Accounting for low energy photons by collecting the energy in a cluster around the muon would be spoiled by calorimeter noise and energy resolution.

In the  $\mu^+\mu^-$  sample, an electromagnetic cluster originating from a radiated  $\gamma$  close to a muon track, could be mis-identified as an electron. Fig. 14 shows the distribution of the angular distance  $\Delta R$  of the false electron from the muon. In the following analysis, electrons inside a cone of  $\Delta R < 0.001$  from muon track are considered as mis-identified IB photons, and recovered. With this procedure, 166 IB photons are recovered in the sample.

In conclusion we can identify a  $\gamma$  as radiated from the lepton if the following conditions are fulfilled:

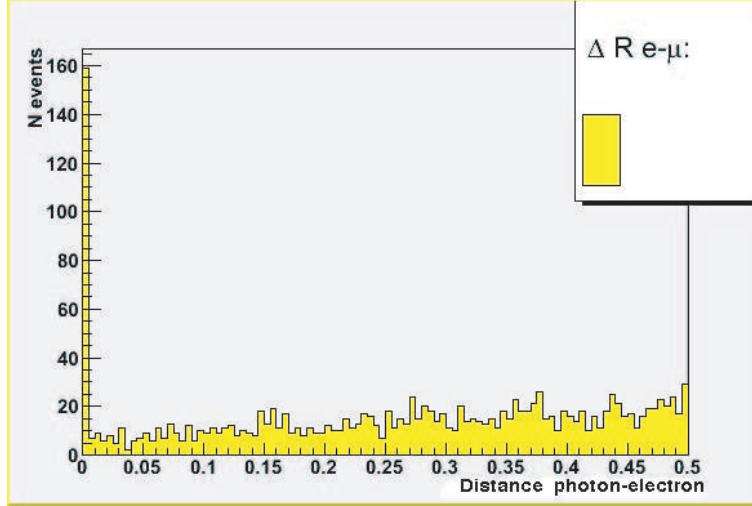


Figure 14: Minimum angular distance electron-muon (see text), in  $bb\bar{Z} \rightarrow \mu^+\mu^-$ , at particle level.

- **IB photons** are reconstructed *only* for the events with at least two leptons reconstructed in the detector, in the fiducial volume  $|\eta| > 2.5$  and with transverse momentum  $P_T > 10$  GeV and at least a photon with  $E_T > 5$  GeV reconstructed inside a cone  $\Delta R < 0.15$  for muon and  $\Delta R < 0.25$  for electron around the track.

	$bbZ \rightarrow \mu^+\mu^-$	$bbZ \rightarrow e^+e^-$
$N_{gen}$	590575	586382
$N_{reco}$	364756	273780
$N_{reco}(\gamma = 0)$	362372	271535
$N_{reco}(\gamma = 1)$	2378	2228
$N_{reco}(\gamma = 2)$	6	17
$N_{gen}(\gamma = 3)$	0	0

Table 2: Number of *bremstrahlung*  $\gamma$  reconstructed.

In Table 2, the reconstructed events are listed, according to the number of  $\gamma_{\text{brem}}$  reconstructed. The sample of events is reduced to 61.7 % of generated events for muon sample and 46.7 % for electron, due to detector acceptance and selection cuts on the lepton  $P_T$  and  $|\eta|$  range, (Section 5.1). 99% of the events reconstructed in both samples are without a separated  $\gamma_{\text{brem}}$  reconstructed. In the muon sample, 7% of IB photons are recovered from mis-identification as electrons.

In conclusion, the IB effect is more important in the electron sample. However, the  $\gamma_{\text{brem}}$ , if emitted close to the electron, constitutes with the electron an unique electromagnetic cluster and the number of photons reconstructed separately is  $\sim 1\%$ . The same percentage of reconstructed photons holds for the muon sample.

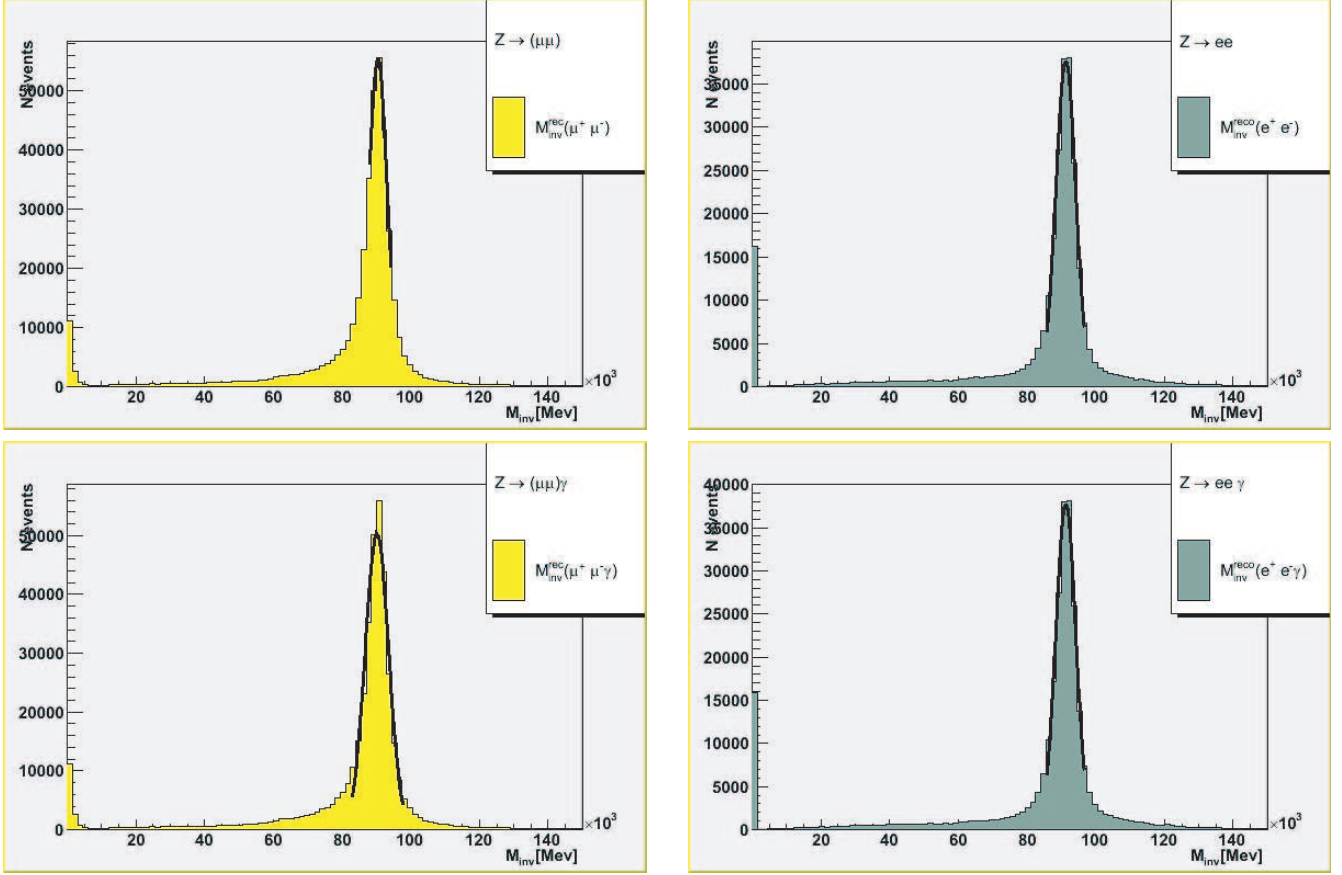


Figure 15: At reconstruction level: distributions of the reconstructed invariant mass  $M_{\mu^+\mu^-}$ ,  $M_{e^+e^-}$  (top). The same distributions after including the IB corrections (bottom). The gaussian fit is shown as a solid line.

## 6 Results

The effect of IB photons reconstructed as separate electromagnetic clusters has been studied for the invariant mass distribution for both the electron and the muon sample. It should be reminded that our samples are  $b\bar{b}Z \rightarrow \mu^+\mu^-$  or  $b\bar{b}Z \rightarrow e^+e^-$ . In those events where a semileptonic b decay occurs with the same flavour as one of the Z decay products, more than one invariant mass combination is possible, namely three. Often, the value of  $M_{\text{inv}}$  associated to this combination of one lepton originating from Z and another one from b decay sits far from  $m_Z$ . Only opposite charge muon pair are considered for invariant mass combinations. The higher efficiency in muon detection increases the number of *fake* combinations in the muon sample.

The invariant mass distributions of  $e^+e^-$  and  $\mu^+\mu^-$  from Z decays are reported in Fig. 15 for the full sample of selected events of both channels (Section 5), without correction for IB photons (top), and with the correction (bottom), which is obtained by summing their four-momentum to the one of the lepton from which they were radiated.

This effect concerning a little percentage of event is clearly not visible in the full sample, but it is interesting to investigate the events with a probable IB photon, to control the validity of the method. In Fig. 16, only those events are plotted.

The correction for IB photons is effective in this sub-sample shifting the events on the tail

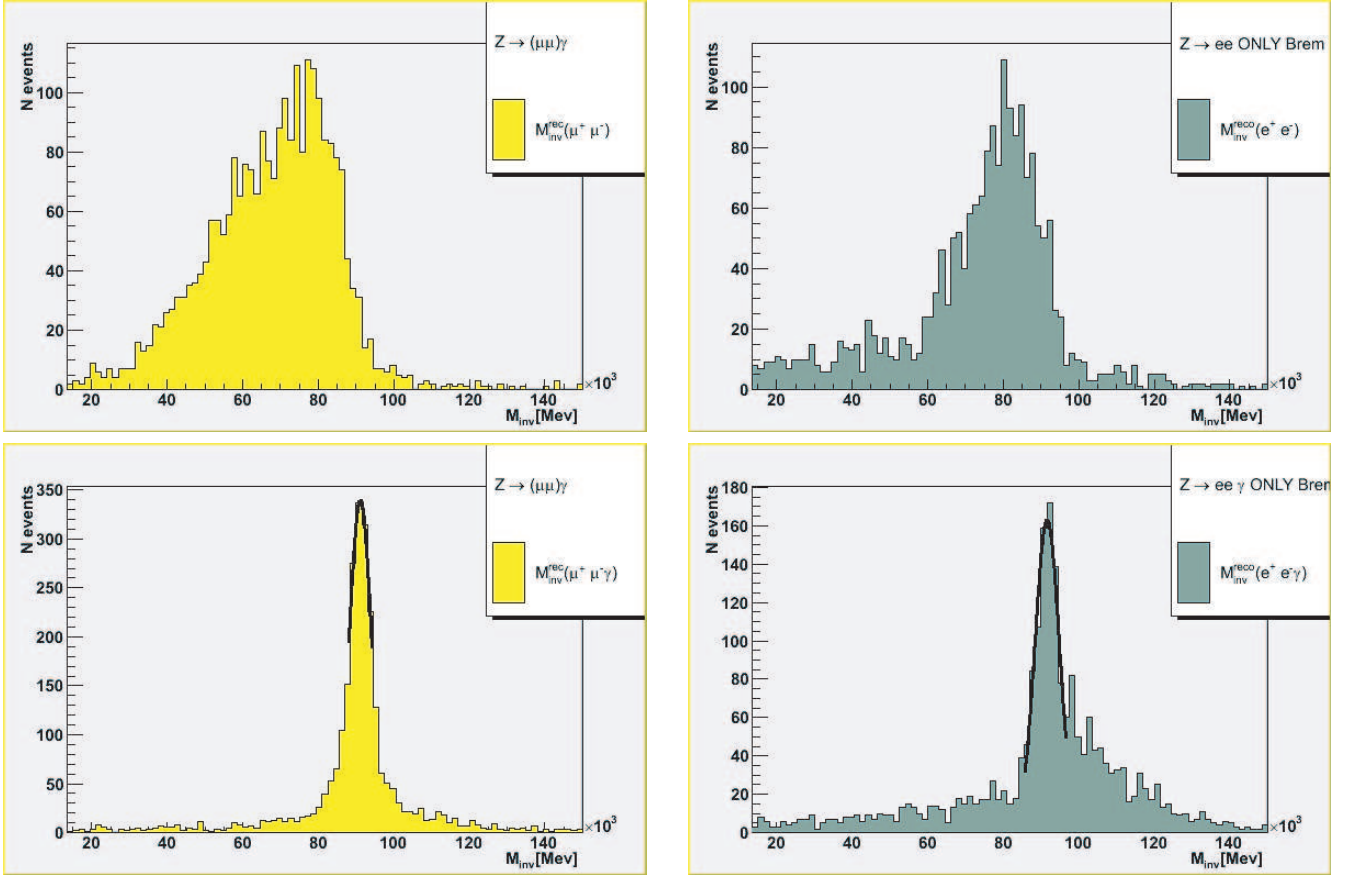


Figure 16: At reconstruction level: distributions of the invariant mass  $M_{\mu^+\mu^-}$ ,  $M_{e^+e^-}$ , for events containing at least a one IB photon ( top). The same quantities after correcting for the reconstructed IB photons(bottom).

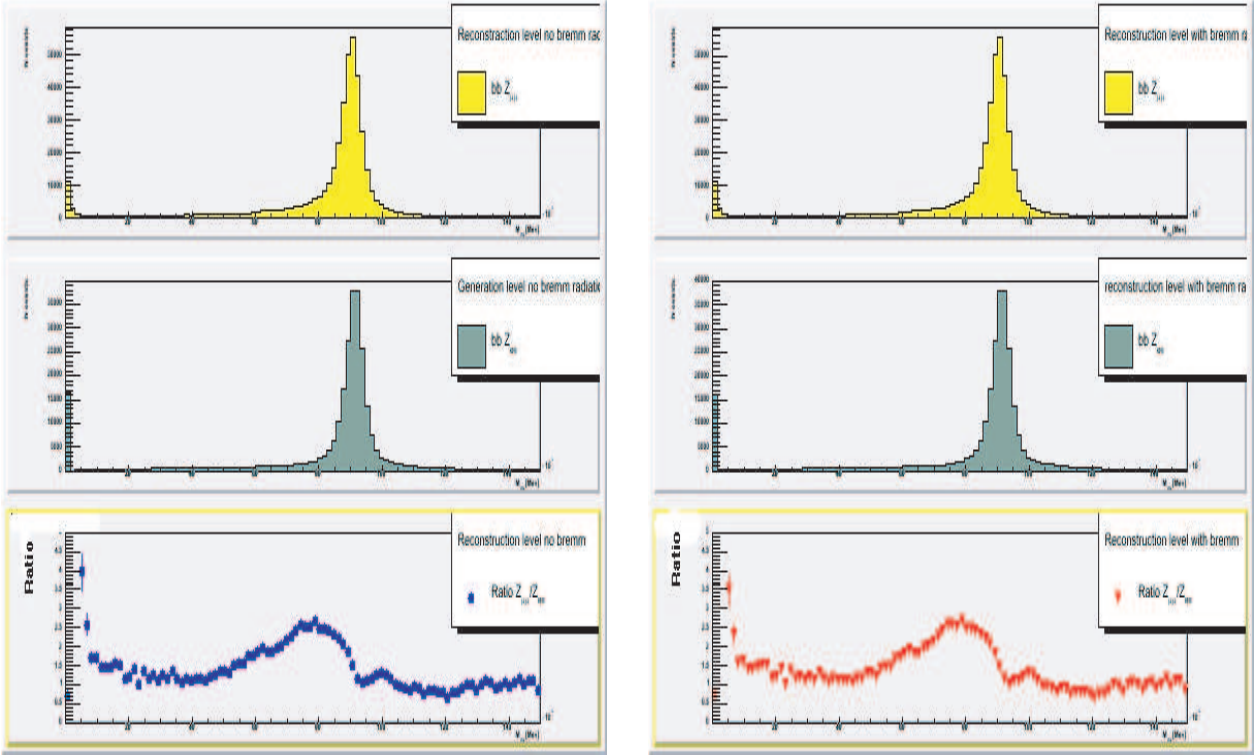


Figure 17: Distributions of invariant mass  $M_{\mu^+\mu^-}$ ,  $M_{e^+e^-}$ , and their ratio for all reconstructed events, before correcting for the IB photons (left) and after correction (right) .

towards the Z mass. The purpose of the gaussian line is to drive the reader's eye. This method apparently corrects better the muon than the electron sample, because an IB photon in this sample is mostly reconstructed as a unique cluster with the electron.

Fig. 17 shows the invariant mass distributions of  $\mu^+\mu^-$  and  $e^+e^-$  and their ratio for the whole sample before adding the IB photons (left); the same quantities after the IB correction are also shown (right).

The ratio higher than unity in the mass region below  $m_Z$  can be explained as the number of events with IB photons reconstructed as separated clusters is higher in the muon than in the electron sample, where they are mostly absorbed in electron clusters. A difference on reconstruction efficiency between muons and electrons explains an additional 15% of difference (Tab.2), together with the higher number of muons reconstructed from b decays, giving origin to *fake* combinations. The structure around Z peak is in large part due to the different detector resolutions between electrons and muons.

In most of the events of the  $e^+e^-$  sample, the IB radiation is taken in account in the energy measured in the calorimeter, because only one cluster is reconstructed and the combined four momentum is measured. The correction to the rest of the sample is negligible. The ratio is a quite regular function of  $M_{inv}$  in the region of our interest between 97.5 GeV and 140 GeV allowing the use of the  $e^+e^-$  sample as control sample with reasonable correction factors. This can be seen, clearly, in Fig.18 where the two ratio distributions (bottom of Fig. 17) are reported overlaid. A straight line is drawn for reader's eye.

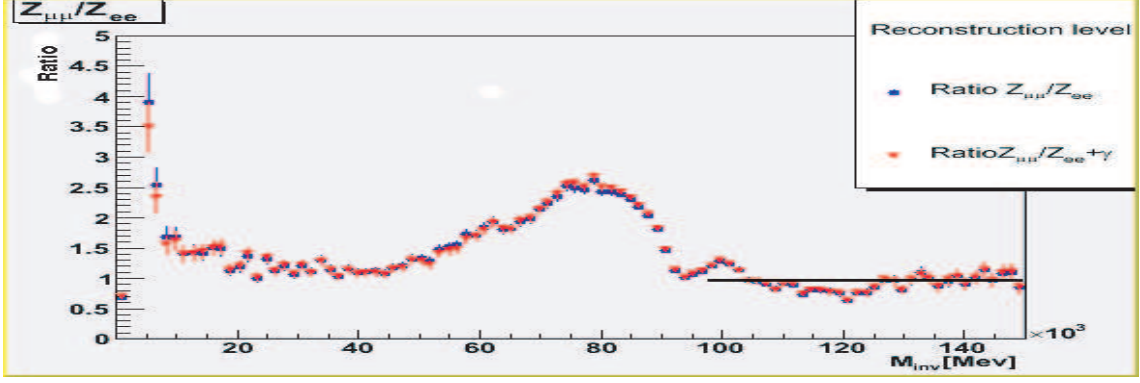


Figure 18: Ratio between the number of events decaying in  $\mu^+\mu^-$  and the number of events decaying in  $e^+e^-$ ,  $\left(\frac{N_{Z\rightarrow e^+e^-}}{N_{Z\rightarrow\mu^+\mu^-}}\right)$ , before IB correction (blue symbols), and after (red symbols). All events of the reconstructed sample are included. The black solid line is for viewing purposes.

## 7 Conclusions

In this paper a strategy based on combined use of Monte Carlo and experimental data to correctly predict a background at LHC is presented. In particular, the study of the associated Z production and decay in the channel  $b\bar{b}Z \rightarrow \mu^+\mu^-$  has been studied using a control sample of  $b\bar{b}Z \rightarrow e^+e^-$  events. The effect of IB radiation has been investigated and corrected for; the impact in the event reconstruction is not large. The ratio of the number of reconstructed events from the two samples in the region of mass higher than  $m_Z$ , interesting for new physics search, is stable and does not imply large correction factors.

## 8 Acknowledgments

We wish to thank Prof. Maria Fidecaro for the helpful discussion and critical reading of manuscript.

## References

- [1] S.Gentile, M.Paniccia, P.Violini, Search for supersymmetric neutral Higgs  $h$  in the decay  $\rightarrow \mu^+\mu^-$  in ATLAS detector at LHC, 2003, Università La Sapienza, Sez. I.N.F.N., Roma, Italy, ATL-PHYS-2003-015.
- [2] ALEPH, DELPHI, L3, OPAL, Search for neutral MSSM Higgs bosons at LEP, 2006, hep-ex/0602042.
- [3] H.Bilokon, V.Chiarella, S.Gentile, G.Nicoletti, Search for supersymmetric neutral Higgs decaying to a  $\mu^+\mu^-$  pair in ATLAS detector at LHC, 2006, *in preparation*,.
- [4] M.A. Dobbs, *et al.*, Les Houches guidebook to Monte Carlo generators for hadron collider physics, 2004, hep-ph/0403045.
- [5] B. P. Kersevan and E. Richter-Was, The Monte Carlo event generator AcerMC version 2.0 with interfaces to PYTHIA 6.2 and HERWIG 6.5, 2004, hep-ph/0405247.
- [6] T. Sjostrand, L. Lonnblad and S. Mrenna, PYTHIA 6.2: Physics and manual, 2001, hep-ph/0108264.
- [7] ATLAS Coll, ATLAS detector and Physics Performance: Technical Design report, volume 2, LHCC 99-15, CERN, 1999.
- [8] S. Agostinelli *et al.*, Nucl. Instrum. Methods Phys Res. A 506 (2003) 250.
- [9] J. Alison *et al.*, IEEE Transactions on Nuclear Science 53 No.1 (2006) 270.
- [10] O. Linossier, L. Poggioli, Final state inner-bremsstrahlung effects on  $H^0 \rightarrow ZZ^* \rightarrow lll$  channel with ATLAS, 1995, LAPP, Annecy-le-Vieux, France, CERN, Geneva, Switzerland, ATLAS Internal note, Phys No 075.